PAPER

Check for updates

Exploiting anion and cation redox chemistry in lithium-rich perovskite oxalate: a novel next-generation Li/Na-ion battery electrode†

Atin Pramanik, [ID] [a] Alexis G. Manche, [a,b] Rebecca Clulow, [ID] [a,c] Philip Lightfoot [ID] *[a] and A. Robert Armstrong [ID] *[a,b]

The fundamental understanding of electrochemical reaction kinetics for lithium/sodium-ion batteries (LIBs & NIBs) is a significant criterion for advancing new-generation electrode materials. Herein, we demonstrate a novel lithium-rich perovskite oxalate $KLi_3Fe(C_2O_4)_3$ (KLFC) cathode with the combination of cation and anion redox delivering discharge capacities of 86 and 99 mA h g^{-1} after 100 cycles for a LIB and NIB, respectively, with good cyclability. Experimental Raman spectroscopy analysis combined with DFT calculations of charged/discharged samples illustrate the oxalate anion redox activity. Further, first-principles calculations of the partial density of states and Bader charges analysis have also characterised the redox behaviour and charge transfer during the potassium extraction processes.

Introduction

With the rapid depreciation of fossil fuels, developing alternative sustainable energy storage devices is needed. In the search for an alternative energy storage system, the rechargeable battery has achieved the most attention due to its high energy density and long cycle life. To fulfil the current practical demands, it is necessary for significant improvement by finding new electrode materials. In this work, sodium-ion battery (NIB) technology is considered an emerging candidate due to the low cost and natural abundances for large-scale applications, in comparison to lithium-ion batteries (LIB).[1] However, enhancing the capacity is an essential objective of electrode development. Moving beyond the conventional paradigm of metal-centred redox activities to search for redox-active anions is a promising approach to increase the capacity and energy density.

A range of cathode materials have been exploited, such as layered transition metal oxides, olivine type, NASICONs, organic cathodes and other polyanionic compounds.[2]

Na_xTMO_2 (TM: transition metal) is the general formula of transition metal oxides (TMOs).[3] TMOs are usually P2 ($0.6 < x < 0.7$, where x denotes the sodium stoichiometry) with trigonal prismatic sodium coordination or O3 type (where $x \approx 1$) with elongated octahedral sodium coordination. The ABBA and ABCABC stacking sequences correspond to P2 and O3 type, respectively, with capacity >100 mA h g^{-1} with good cycle stability and electronic conductivity.[4] The organic cathode materials are easy to synthesise and are low-cost and environmentally friendly but have poor energy density and electronic conductivity.[5] The olivine and NASICON type compounds with general formula $NaMPO_4$ (M = Fe, Mn) $Na_xMM'(PO_4)_3$ (M and M' = V, Ti, Cr, Fe, Co, Ni etc.) respectively have been explored widely.[6] Among the polyanionic compounds, mostly phosphate, pyrophosphate, sulfate, silicate and borate based materials have been explored.[7] Several of these materials suffer from poor long-term cycling stability.[6,8] Polyanionic compounds have a high inductive effect and stable frameworks due to strong covalent bonds, resulting in higher and tuneable operating voltages. These include $NaFePO_4$,[9] $NaVPO_4F$,[10] $Na_4Mn_3(PO_4)_2(P_2O_7)$,[11] A_xMSO_4F (A = Li/Na; M = 3d metals), $Li_3V_2(PO_4)_3$,[12] $Na_2Fe_2(SO_4)_2$[13] etc., which possess acceptable thermal stability, long cycle life and high rate durability. In the search for new polyanions, the oxalate $(C_2O_4)^{2-}$ anion represents an interesting alternative. The acidity of oxalic acid lies in between sulfuric acid and phosphoric acid. The electronegativity of these conjugate bases follows this sequence $(SO_4)^{2-} > (C_2O_4)^{2-} > (PO_4)^{3-}$. Oxalate can act as a mono-, bi-, tri- or tetra-dentate ligand and form simultaneously mono- or poly-nuclear metal complexes. Tarascon et al. first tested

[a]*School of Chemistry, University of St Andrews, KY16 9ST Scotland, UK.*
E-mail: pl@st-andrews.ac.uk, ara@st-andrews.ac.uk
[b]*The Faraday Institution, Quad One, Harwell Science and Innovation Campus, Didcot, OX11 0RA, UK*
[c]*Department of Chemistry – Ångström Laboratory, Uppsala University, Box 538, 751 21 Uppsala, Sweden*

†Electronic supplementary information (ESI) available: SEM images, differential capacity plot for NIBs and LIBs, *ex situ* XPS of LIB, Raman data for pristine and raw electrode. See DOI: https://doi.org/10.1039/d2dt01447e

$Na_2Fe(C_2O_4)_2 \cdot 2H_2O$ as a cathode material *versus* Li/Li^+ between 2.0 and 4.2 V at a rate of C/10, achieving a specific capacity of 35 mA h g^{-1} at an average potential of 3.3 V.[14] Following on from this, our group has explored additional oxalate-based polyanionic systems as positive electrodes for LIB/NIBs, *e.g.*, $Na_2Fe_2(C_2O_4)_3 \cdot 2H_2O$,[15] $Li_2Fe(C_2O_4)_2$,[16] $Na_2Fe(C_2O_4)F_2$,[17] $Na_2Fe(C_2O_4)(HPO_4)$,[18] each of which reveals good cycling stability, with promising energy densities and structural stability.

Inspired by these previous studies, we successfully synthesised $KLi_3Fe(C_2O_4)_3$ (KLFC) using a simple hydrothermal technique. This unusual perovskite-like ("perovzalate") crystal structure has B-site 3:1 ordering of Li, Fe and simultaneous ordering of K vacancies on the A-site.[19,20] This compound has recently been shown to be active as a cathode material for potassium storage.[21] In the present paper we demonstrate its activity for Li and Na storage. Here, we use Raman spectroscopy to illustrate the combination of transition metal cation and oxalate anion redox activity. Further, first-principles calculations have also been used to explain the redox behaviour and charge transfer during the potassium extraction processes.

Experimental

Synthesis of $KLi_3Fe(C_2O_4)_3$

The yellow crystalline sample was synthesised using a simple, previously reported hydrothermal method.[19,21] Ferrous chloride tetrahydrate ($FeCl_2 \cdot 4H_2O$), oxalic acid dihydrate ($C_2H_2O_4 \cdot 2H_2O$), lithium carbonate (Li_2CO_3) and potassium carbonate (K_2CO_3) were placed in a 23 ml Teflon-lined autoclave with the molar ratio of 1.5:4:2:1 as starting materials. Two ml of deionised water was used as a solvent. All the raw materials were used without further purification. The autoclave was sealed immediately and placed in an oven at 190 °C for four days. After natural cooling the crystalline products were washed several times with deionised water and acetone to remove by-products. The yellow crystals were finally dried in an oven at 60 °C for 4 h and stored for further characterisation.

Material characterisation

The as-synthesised samples were characterised by powder X-ray diffraction (PXRD). The crystalline samples were hand ground using a mortar and pestle, and PXRD was recorded using a STOE STADI/P diffractometer with Cu $K_{\alpha 1}$ radiation (λ = 1.5406 Å) in the 2θ range 5–90°, operating in Debye–Scherrer mode. The Rietveld refinement method was used to check the phase purity of the sample using the GSAS package with the EXPGUI interface.[22] The structural model was taken from the single crystal structure, with fixed atomic parameters. Peak shape, background, lattice parameters and preferred orientation (using the spherical harmonics model) were refined. The microstructural features and energy dispersive X-Ray (EDX) elemental analysis were performed using a JEOL JSM-6700F scanning electron microscope (SEM) equipped with a field emission gun (FEG). A tungsten filament electron

source at an accelerating voltage of 15 kV was used to record the secondary images for pristine, ball-milled, and composite samples. Atomic number contrast imaging was recorded using a retractable backscattered electron detector. A Renishaw inVia Qontor confocal Raman microscope was used to measure Raman spectra using a 532 nm laser grating from 100 to 1900 cm^{-1}. The *ex situ* Raman spectra were recorded on cycled pellet electrodes. The electrodes were stopped after ten cycles at the end of charge (at 4.3 V) and discharge (at 1.7 V). The optical cell (EL-Cell) was assembled and sealed inside an Ar-filled glovebox to avoid air exposure.[23] Further, the pellet electrodes were assembled to perform after cycling charge/discharge X-ray photoelectron spectroscopy (XPS). The XPS data were recorded using a Scienta X-ray photoelectron spectrometer with a monochromatic source.

Electrochemical characterisation

Electrochemical characterisation was performed on pellet electrodes. Initially 0.60 g of crystalline sample was ball-milled for 30 min to reduce the particle size. The ball-milled samples were then mixed with 0.30 g of conductive Super C65 carbon black and ball-milled for a further 20 min. The composite samples were then mixed by hand grinding with 0.1 g polytetrafluoroethylene (PTFE) binder to make a homogeneous electrode material. Using a hydraulic hand press, the self-standing pellet electrodes (13 mm diameter and ~0.08 mm thickness) were pressed at 4 tonnes cm^{-2}. The electrodes were dried in a vacuum oven for 12 h before transferring them to the glovebox. The electrodes had an average active mass of ~5–6 mg. CR2325 (NRC Canada) type coin cells were assembled using Na metal as the counter electrode and 1 M $NaClO_4$ in propylene carbonate with 3% fluoroethylene carbonate additive as electrolyte for NIB. The LIB cells were assembled using Li metal as counter electrode and commercial LP30 (1 M $LiPF_6$ in ethylene carbonate : dimethyl carbonate = 1:1) as electrolyte. The electrochemical measurements were performed using a Biologic Macpile II system. The galvanostatic charge/discharge (GCD) experiments were carried out within the voltage window 1.7–4.3 V (*vs.* Na^+/Na) and 2.0–4.4 V (*vs.* Li^+/Li) at rates of 5 and 10 mA g^{-1}. For X-ray photoelectron spectroscopy (XPS) and Raman spectroscopy measurements, the cathode electrodes were prepared in the 75:15:10 weight ratio of KLFC, conductive Super C65 carbon black and PTFE, respectively.

Computational methods

Density functional theory (DFT) calculations based on the plane-wave method were performed with the Vienna *ab initio* simulation package (VASP)[24] using the Perdew–Burke–Ernzerhof (PBE) functional[25] augmented by a Hubbard on-site correction U of 4 eV applied to the Fe 3d states within the generalised gradient approximation (GGA+U).[26] A projected augmented wave (PAW) approach[27] treated core electrons, with the K 1s, Li 1s, C 2p, O 2p, and Fe 2p semi-core states considered valence states. A plane-wave cut-off energy of 520 eV was used for structural optimisations and properties with a 3 × 3 × 2

k-point grid. The atomic positions and unit cells were optimised until all forces converged to 0.001 eV Å^{-1}. Spin-polarised calculations were performed since the magnetic properties of Fe atoms may influence the material electronic structures. Bader charges were calculated to understand the charge transfer between ions related to the redox processes within the structures.[28]

Results and discussion

Single crystals of KLi$_3$Fe(C$_2$O$_4$)$_3$ were manually separated from the bulk sample, and their phase purity was confirmed using powder X-ray diffraction before further measurements. The compound adopts the $R\bar{3}c$ space group with unit cell parameters of a = 11.4420(2) and c = 15.14383(2) Å, as shown in Fig. 1a.[19] The crystal structure consists of an extended framework of corner linked LiO$_6$ and FeO$_6$ octahedra in a perovskite-like structure with 3 : 1 ordering of Li$^+$ and Fe^{2+} at the B site, and 1 : 3 ordering of K$^+$ and vacancies on the A site whilst the oxalate ligands act as bridging anions. The local environment around the K$^+$ site is 12-coordinate, with six K–O bonds at 3.01 Å and six at 3.18 Å.
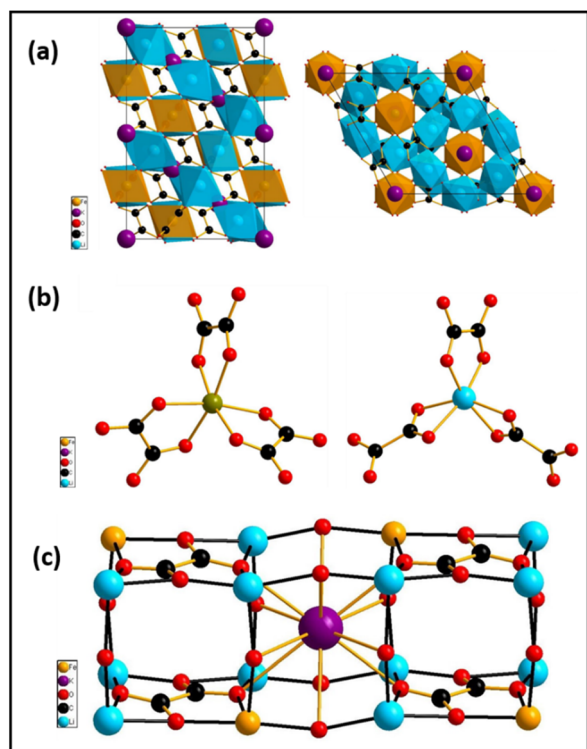
Three oxalate moieties coordinate each B site cation, though the coordination modes differ for the Li and the Fe centres, as shown in Fig. 1b. The BO$_6$ octahedra are linked by oxalate ligands, forming single-atom bridges, Li–O–Li and Li–O–Fe. Each of the cations lies on special positions within the unit cell with Wyckoff positions/site symmetries: K$^+$ (6b, $\bar{3}$); Fe^{2+} (6a, 32) and Li$^+$ (18e, 2). There is little likelihood of Li$^+$ ion mobility due to the tight coordination environment around these small octahedral B-sites. In contrast, due to the strict ordering of K$^+$ and vacancies on the A-sites, the cuboidal A-sites containing K$^+$ ions are surrounded by face-sharing to six vacant cuboids, as shown in Fig. 1c. These vacant A-sites are each capped on two opposite faces by oxalate groups. In principle, this gives rise to free channels throughout the structure by which alkali cation migration can occur, albeit with some restrictions caused by the capping oxalate moieties. The phase purity of the hand-ground pristine powder sample was confirmed by Rietveld refinement analysis (Fig. 2).

XPS analysis was conducted to understand the oxidation state of the metal centre of the KLFC sample. The XPS spectra of KLFC pristine compound for Fe 2p, K 2s, O 1s, and C 1s are shown in Fig. 3. The deconvolution of the Fe 2p core-level spectrum shows Fe 2p$_{3/2}$ characteristic peaks at binding energy 710.5 (Fe^{2+}) to 713.1 eV (Fe^{3+}) with corresponding satellite peak, which is related to Fe 2p$_{3/2}$ (Fig. 3a).[29] The peak intensities confirm that the compound contains mostly Fe^{2+} with a small amount of Fe^{3+}, which could come from the surface oxidation of the sample, which is not uncommon for such materials.[29,30] The K 2s peak is located at a binding-energy of 378.2 eV, shown in Fig. 3b.[31] The deconvolution of the O 1s spectra shows three peaks (Fig. 3c). The prominent peak at 532.5 eV arises from the O–C=O of the oxalate ligand. The other two peaks at a binding energy of 530 and 534.2 eV correspond to C=O and O–C=O, respectively.[32] The C 1s spectrum was fitted with six components, as shown in Fig. 3d. The
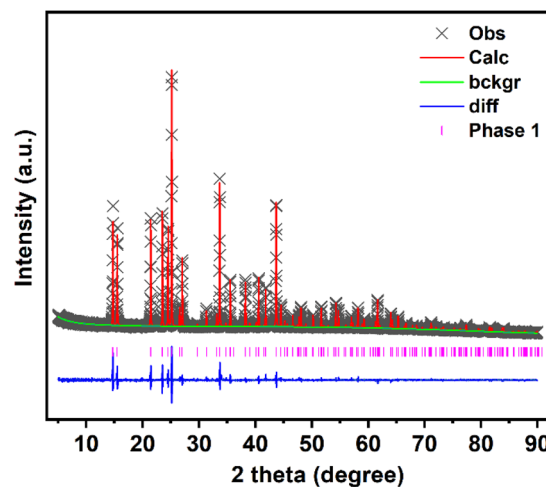

Fig. 1 (a) The crystal structure of KLi$_3$Fe(C$_2$O$_4$)$_3$ viewed along the a and c directions. (b) Coordination environments of Fe^{2+} and Li$^+$ sites in KLi$_3$Fe(C$_2$O$_4$)$_3$. Fe–O and Li–O bond lengths are 2.12 Å and 2.02–2.18 Å, respectively. (c) Detail of the cuboidal A-site cavity occupied by K$^+$. This site shares all six faces with vacant A-sites, which are themselves capped on two opposite faces by oxalate moieties. For clarity, only two adjacent vacant sites are shown. K: purple, Li: turquoise, Fe: orange, O: red.

Fig. 2 Rietveld refinement analysis of hand-ground, powdered pristine sample at room temperature, lattice parameters are a = 11.4222(1) Å, c = 15.14383(2) Å, space group $R\bar{3}c$ wR_p = 0.0339, R_p = 0.0369, χ^2 = 4.545.
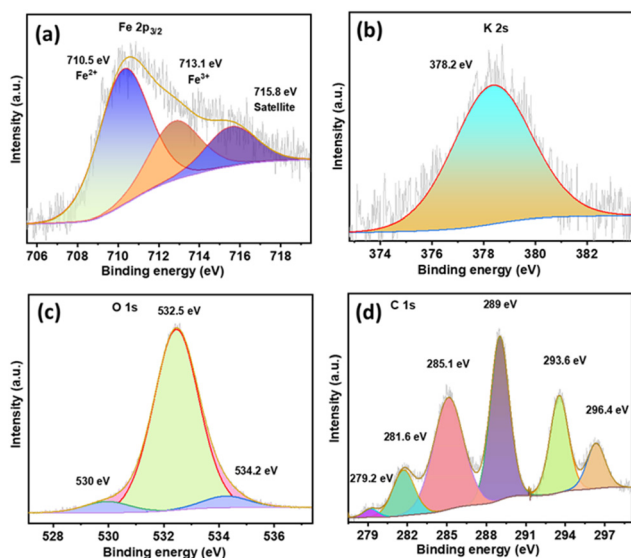
Fig. 3 X-ray photoelectron spectroscopy (XPS) characterisation of pristine KLFC compound, (a) Fe 2p, (b) K 2s, (c) O 1s, and (d) C 1s.

main three peaks at a binding energy of 285.1, 289, and 293.6 eV represent C–C, C=O, and O=C–O, respectively.[33] In addition, a weak peak at 296.4 eV was recognised as the satellite peak connected with a $\pi \rightarrow \pi^*$ transition.[34] The other two peaks at a lower binding energy of 279.2 and 281.6 eV could arise from the interaction between potassium and lithium with carbon, respectively.[35] The XPS analysis supports the phase purity of the sample, as derived from the Rietveld analysis.

The microstructure of the hand ground KLFC sample was investigated by scanning electron microscopy (SEM). Fig. S1a and b, ESI† show SEM images of the parent compound under low and high magnification respectively, with an average particle size of ~50–55 μm. Ball-milling for 30 min was performed using a Fritsch Pulverisette 8 mill, and the average particle size was reduced to ~1–1.5 μm (Fig. S1c, ESI†). Addition of conductive Super C65 carbon to increase the conductivity, followed by another 30 min ball-milling, gave the composite shown in Fig. S1d, ESI.†

Galvanostatic charge–discharge (GCD) experiments were performed to explore the electrochemical performance of KLFC in the potential window 1.7–4.3 V for NIB. The differential capacity plots for the 2nd, 5th, and 100th cycles at a rate of 10 mA g^{-1} are shown in Fig. 4a. There are three pairs of oxidation/reduction peaks present at 3.1/2.73, 3.5/3.25, and 3.83/3.53 V. During the initial few cycles, the capacity was low, with high cell polarisation. However, after a few cycles, the reversible capacity progressively increased and reached 99 mA h g^{-1} after 100 cycles. The gradual increase of reversible capacity is probably due to the electrochemical grinding effect, which enhances enables faster ion transfer. A discharge capacity of 55 mA h g^{-1} was observed after 100 cycles when applying a 10 mA g^{-1} current rate (Fig. 4b). Fig. S2, ESI† shows the differential capacity plots for the 10th, 15th, and 50th cycles at 10 mA

Fig. 4 Half-cell electrochemical performance of KLFC in NIBs. Differential capacity plots of (a) 2nd, 5th, and 100th cycles at 1.7–4.3 V potential window and 10 mA g^{-1} current rate. (b) Cycling performance at (i) 5 and (ii) 10 mA g^{-1} current rate with coulombic efficiency at 5 mA g^{-1}. (c) Galvanostatic voltage profiles with capacity plots of the 15th, 50th, and 100th cycles.

g^{-1}, which clearly shows three pairs of redox peaks with progressive diminution of cell polarisation. Galvanostatic voltage profiles of the 15th, 50th, and 100th cycles are shown in Fig. 4c, which align with the differential capacity plots (Fig. 4a and S2, ESI†). The voltage profile corresponds to ~0.65 Na$^+$ ions exchanged per formula unit within the 1.7–4.3 V potential window (Fig. 4c). An electrochemical performance comparison table with other polyanionic systems is shown in Table S2, ESI.†

GCD tests were performed over the potential window 2.0–4.4 V at a rate of 10 mA g^{-1} to check performance in LIBs. The dQ/dV profile of the 2nd, 5th and 100th cycles clearly show three pairs of oxidation/reduction peaks at 3.18/3.07, 3.46/3.43, and 3.86/3.81 V, shown in Fig. 5a. The first cycle discharge capacity of the KLFC electrode was 77 mA h g^{-1}, with only 48% coulombic efficiency. The reversible capacity decreased over
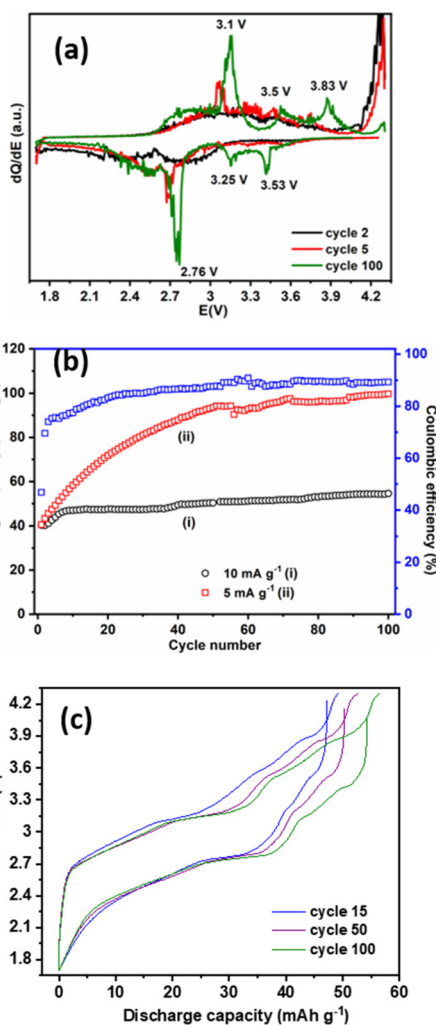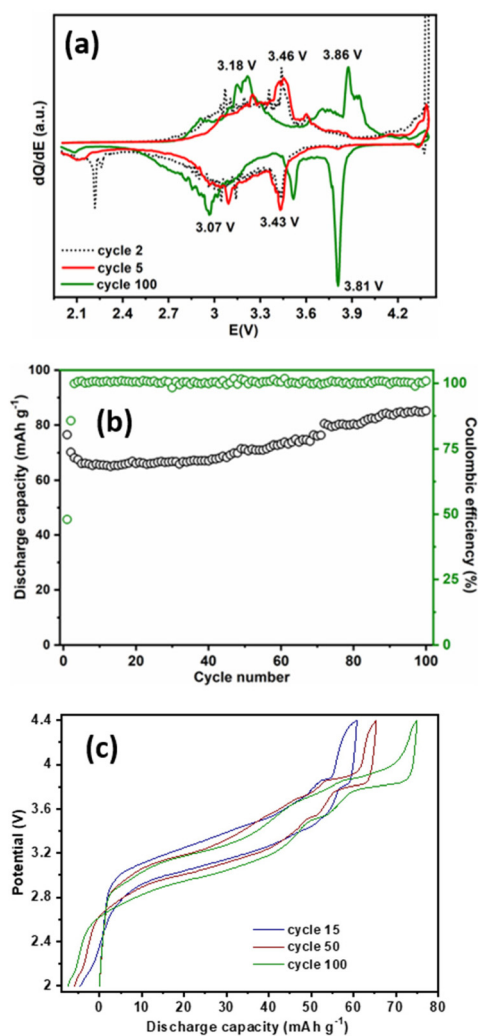
Fig. 5 Half-cell electrochemical performance of KLFC in LIBs. Differential capacity plots of (a) 2nd, 5th, and 100th cycles at 2.0−4.4 V potential window at 10 mA g^{-1} current rate. (b) Cycling stability at 10 mA g^{-1} current rate with corresponding coulombic efficiency. (c) Galvanostatic voltage profiles with capacity plots of the 15th, 50th, and 100th cycles.

Fig. 6 Electrochemical NIB storage mechanism by XPS analysis of KLFC electrode. XPS spectra of (a) Fe 2p and corresponding ratios of Fe^{2+} and Fe^{3+} for composite, charged and discharged samples, (b) Na 1s for charged and discharged state.

peak at 713.1 eV, suggesting partial oxidation and an increase in Fe^{3+}. Similarly, in the fully discharged state, the increased peak at 710.5 eV confirms the reduction of Fe^{3+} to Fe^{2+}. It is also interesting to note that the peak intensity of the Na 1s spectrum in the discharged state (binding energy 1072 eV) is much higher than that in the charged state (Fig. 6b) due to the removal of Na$^+$ on charge.[36,37] The prominent Na 2s signal was observed at lower-binding energy in the discharged state (1069.9 eV), which could be due to the formation of Na$^+$ bonded to an oxygen atom.[37] This suggests reversible Na$^+$ insertion/extraction during the GCD process. Significantly, the valence state transformation of iron is insufficient to account for the observed specific capacity. This implies that another electrochemical process must be involved during the charge/ discharge process.

In order to understand the charge-storage mechanism of the KLFC electrode, *ex situ* Raman spectroscopy measurements were carried out. Fig. S5 and S6, ESI† shows the Raman spectra of pristine KLFC and the raw electrode. The prominent intense peak at 1479 cm^{-1} was assigned to the (C=O) stretching vibration of the oxalate ligand.[16] The peak at 916 cm^{-1} can be ascribed to ν(C–C) stretching. These two primary vibrations were observed in both pristine and raw electrode samples. Furthermore, due to the addition of carbon additive in the electrode sample, two strong broad peaks were observed at 1348 and 1597 cm^{-1}, corresponding D and G bands, respectively. The D band originates due to the structural defects caused by the hybridisation of carbon atoms, whereas the G band replicates the stretching motions between sp^2 hybridised carbon atoms.

Spectra were obtained after ten cycles in both the charged and discharged states to understand the redox mechanism in

the first fifteen cycles before increasing, reaching 86 mA h g^{-1} after 100 cycles (Fig. 5b). The differential capacity plots for the 10th, 15th, and 50th cycles are shown in Fig. S3, ESI† showing that the multi-step delithiation/lithiation processes were retained. The reversible capacity demonstrates that ∼1 Li$^+$ ion can be reversibly extracted from the KLFC electrode during delithiation, Fig. 5c.

The electrochemical redox mechanism was analysed by *ex situ* XPS analysis (Fig. 6). Fig. 6a presents the XPS spectra of composite, 10th cycle fully charged and discharged samples (Fig. 6a) for NIB and Fig. S4, ESI† for LIB. In the composite sample, Fe^{2+} (binding energy 710.5 eV) is dominant, with a smaller amount of Fe^{3+} (binding energy 713.1 eV), which could arise from surface oxidation of the KLFC sample. The 10th cycle fully charged state sample shows a strengthening of the
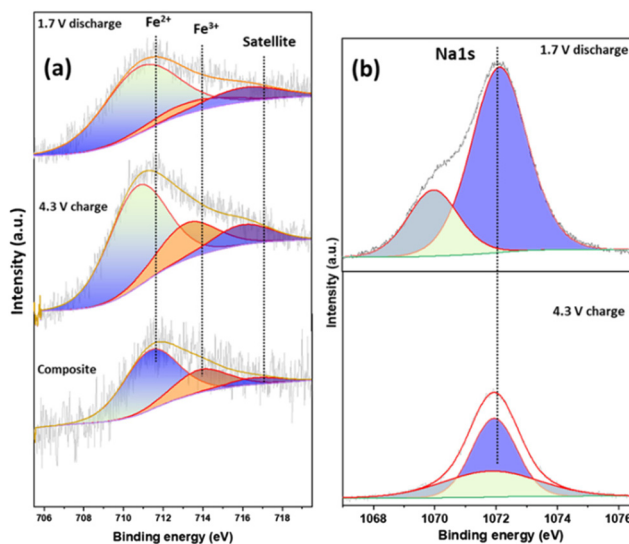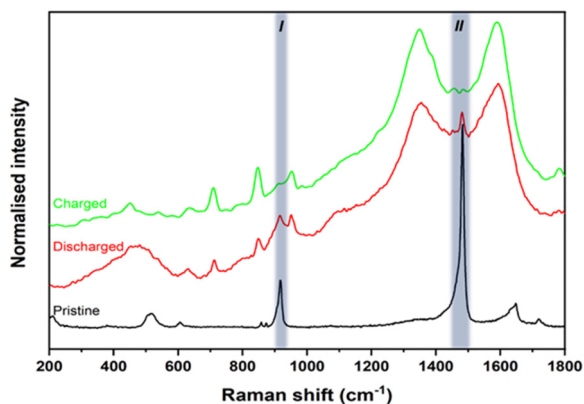
Fig. 7 *Ex situ* Raman spectra at fully charged (green) and discharged (red) states of cycling electrodes after 10 cycles and Raman spectra of pristine KLFC (black).

NIB (Fig. S5, ESI†). Fig. 7 shows Raman spectra of the charged (green) and discharged (red) electrodes in *ex situ* cells, and pristine KLFC (black). The different Raman peak assignments of pristine KLFC are reported in Fig. S6, ESI† and Table S2, ESI.† In Fig. 7, the principal peak II at ~1480 cm⁻¹, corresponding to C=O asymmetric stretching in the oxalate group, is prominent in the discharged state. In contrast, it is essentially absent in the charged state. Comparing the intensity of the spectra, the evolution with the state of charge confirms a

significant loss of intensity in the charged state, which means that the C=O double bond becomes more robust and more localised at discharge state. The other characteristic peak I at ~918 cm⁻¹ is assigned to C–C symmetric stretching. Similar to peak II, this peak also becomes weaker in the charged state, indicating that the concentration of C–C group is decreasing and gives further evidence of geometry changes of the oxalate group between the charged and discharged states. The *ex situ* Raman spectroscopy analysis is consistent with oxalate anion redox during charge/discharge without CO₂ evolution.¹⁶ The other vibrational peaks related to oxalate at lower wavelength were not prominent in the charged/discharged samples due to the poor crystallinity, which is common for *ex situ* samples.

To further understand the redox behaviour in KLFC, various DFT calculations were also performed. The results of the calculated lattice parameters transform from *a* = 11.533 Å, *b* = 11.527 Å, *c* = 15.403 Å, to *a* = 11.426 Å, *b* = 11.426 Å, *c* = 15.814 Å, after full extraction of K⁺ ions from the KLFC structure (Fig. 8a). During the geometry optimisation step, ionic positions, cell volume, and cell shape are allowed to change. This is the reason why the values of *a* and *b* axes can deviate very slightly from each other (<0.1 Å) from the initial to final state. However, the difference being so small, we still consider the unit cell conserves the *R3̄c* space group. The shrinkage along the *a* and *b* axes is largely compensated by the enlargement along the *c* axis (Fig. 8b), which gives a volume change of only 0.8% after removing all the K⁺ ions. This last observation
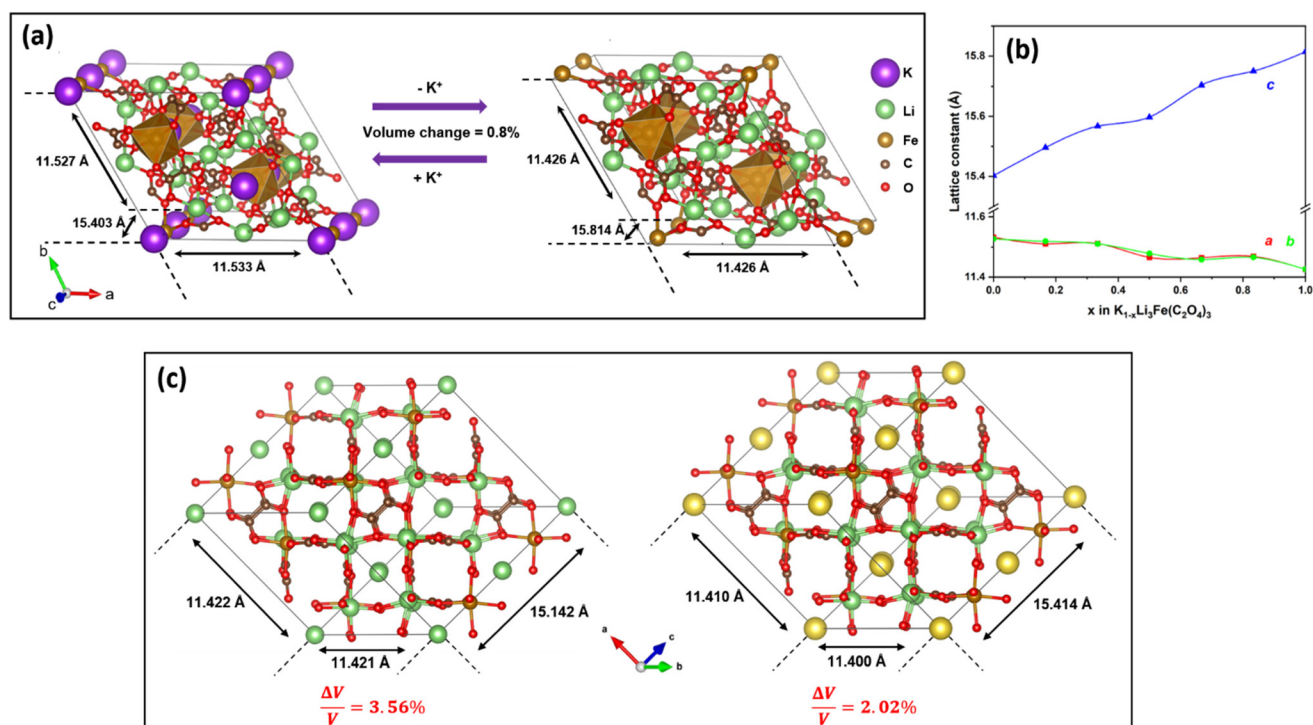

Fig. 8 Calculated unit cell of KLi₃Fe(C₂O₄)₃ with full and empty K⁺ ion sites 4 corresponding respectively to discharged and charged states (a). The lattice parameter change of K₁₋ₓLi₃Fe(C₂O₄)₃ as a function of the state of charge *x* (b). Optimised unit cells of respectively LiLi₃Fe(C₂O₄)₃ and NaLi₃Fe(C₂O₄)₃ by replacing K⁺ ions by Li⁺ ions on the left-hand side and by Na⁺ ions on the right-hand side (c).
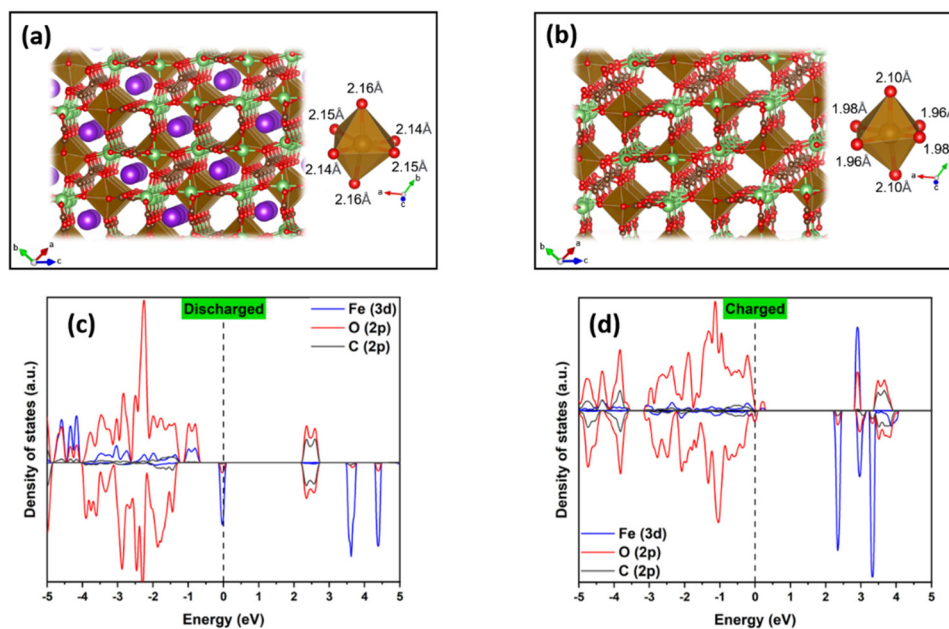
Fig. 9 Atomic structures of $K_{1-x}Li_3Fe(C_2O_4)_3$ in the pristine (a) and fully-charged (b) states based on DFT calculations, and their corresponding partial density of states (PDOS) for discharged (c) and charged (d) states. The Fermi level is set at 0 eV.

suggests that this characteristic could reduce the possibility of crack formation during cycling. Fig. 9a–c shows the structural evolution at different states of charge based on DFT calculations, including changes in the atomic structure of FeO_6 octahedra. All Fe–O bonds shrink after removal of K^+ ions from the structure, about ~0.17 Å for four of them and only ~0.06 Å for the other two contained in an FeO_6 octahedron. This seems to be due to the enlargement of the c axis when the K sites have been emptied and which makes it possible to compensate for the shrinkage of these two Fe–O bonds. This study focuses on the cases of Na and Li storage, hence the optimised structures of $LiLi_3Fe(C_2O_4)_3$ and $NaLi_3Fe(C_2O_4)_3$ were derived from the initial KLFC system to check whether this induced significant changes in the lattice parameters or the symmetry of the structure. Fig. 8c shows the structures optimised by DFT calculations of $LiLi_3Fe(C_2O_4)_3$ and $NaLi_3Fe(C_2O_4)_3$, the ionic radii of Li^+ (0.76 Å) and Na^+ (1.02 Å) being smaller than that of K^+ (1.38 Å), induces slight shrinkage of the unit cells without any major change in symmetry or atomic arrangement within both structures. The volume shrinkage is 3.56% and 2.02% for $LiLi_3Fe(C_2O_4)_3$ and $NaLi_3Fe(C_2O_4)_3$ respectively which are low values compared with e.g. the phospho-olivines $LiFePO_4$ and $NaFePO_4$ which have a volume difference of 6.4% after geometry optimisation by DFT calculations with similar input parameters.[38,39] Thus, we can reasonably conclude that the evolution of the structures $Li_{1-x}Li_3Fe(C_2O_4)_3$, $Na_{1-x}Li_3Fe(C_2O_4)_3$, and $K_{1-x}Li_3Fe(C_2O_4)_3$ would be very similar by gradually removing x ions to simulate electrochemical cycling. In Fig. 9, we also present the spin-polarised partial density of states (PDOS) of the Fe (3d), C (2p) and O (2p) states at the theoretical discharged (Fig. 9d), inter-

mediate (Fig. 9e) and charged (Fig. 9f) configurations. The calculated electronic structures show that the fully-potassium inserted/extracted phases have relatively wide energy gaps of 2.19 eV and 2.21 eV, respectively. These gap values can be considered high and thus demonstrate the poor electronic conductivity existing in KLFC. In the discharged state, we observe three peaks just below the Fermi level. Although the peak of iron is much larger than that of oxygen and carbon, the latter two remain visible. Then, in the charged state, when the potassium ions have all been removed from the structure, the electrons of these three peaks have been oxidised and end up in the conduction band. This observation illustrates the loss of electrons not only on Fe but also on oxalate during the redox process. At the intermediate configuration, the central peak of Fe (3d) and the weak peaks of O (2p) and C (2p) are present around the Fermi level. After further potassium extraction, electrons on the peaks at the Fermi level will shift to the conduction band. Overall, these electron shifts of both Fe and C_2O_4 illustrate that, in this compound, both cationic and anionic redox behaviour is present.

An analysis of Bader charges[28] during the potassium extraction process is also an excellent tool to verify redox behaviour in KLFC. The Bader charge gain relative to the fully potassium extracted phase is shown in Fig. 10a as a function of the potassium ion composition x in the structure. This figure shows that iron ions dominate charge compensation throughout the redox process. However, it is also important to note that oxalate plays a significant role during the potassium extraction process since it is visible that the charge increases on the oxalate group. At each x value of potassium ion composition, the total Bader charge during redox processes is shown by
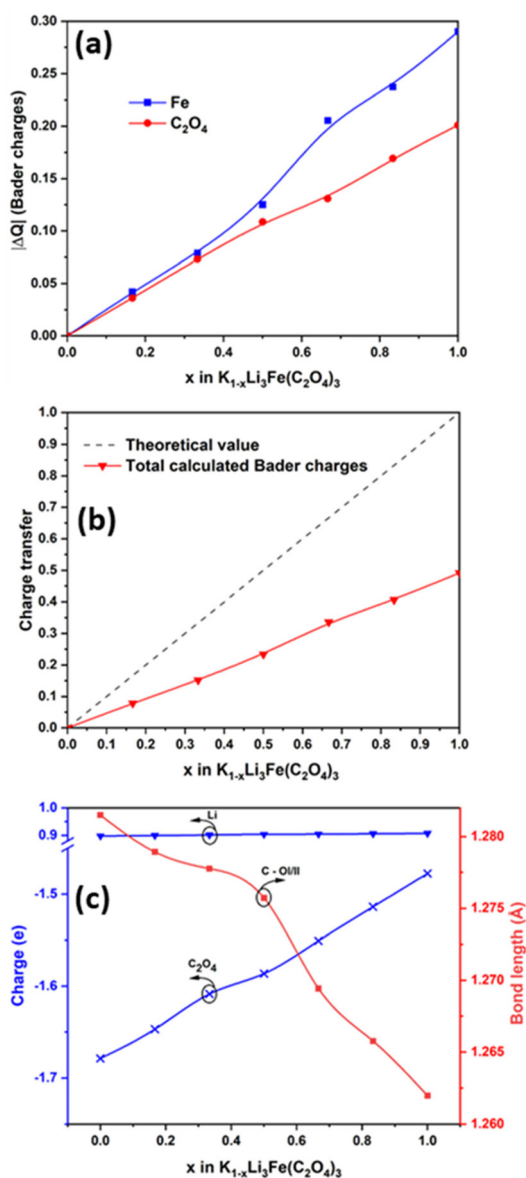
Fig. 10 (a) Bader charges of Fe (blue line) and C_2O_4 group (red line) during the K-ion extraction. (b) Sum of Bader charges from Fe, C, and O ions at different potassium compositions. The red line represents total Bader charges for KLFC, and the dashed line represents the corresponding theoretical values needed for the charge compensation. (c) Averaged charges for Li and C_2O_4 group and calculated average bond length of C–OI and C–OII vs. potassium content in KLFC.

solid lines in Fig. 10b. Once K^+ is removed, the remaining ions (Li, Fe, C and O ions) must contribute an electron to the system in order to compensate charge. The theoretical quantity of electrons required to compensate for the charge loss during potassium removal is represented by the dashed line in Fig. 10b. Therefore, the discrepancy between the solid line and the dashed line indicates the inaccuracy of the Bader charge calculation method. Generally, the Bader charges tend to be smaller than the absolute values due to the localisation/delocalisation phenomenon in charge analysis. Fig. 10c shows

from the calculated Bader charges that the charge on lithium ions is almost constant (value of approx. 0.89). The charge on oxalate varies significantly, and the C–O bond length fluctuates simultaneously with the charge on oxalate, which agrees well with the observations made in the *ex situ* Raman study in the charged and discharged states and gives corroborative evidence of polyanionic redox behaviour in this process.

Conclusions

In summary, an iron-based perovskite oxalate polyanionic compound $KLi_3Fe(C_2O_4)_3$ has been demonstrated as a possible positive electrode material for LIB and NIB application. The compound delivers 86 mA h g^{-1} specific discharge capacity after 100 cycles between 2.0–4.4 V vs. Li^+/Li at a rate of 10 mA g^{-1}. It also delivers 99 mA h g^{-1} after 100 cycles at 5 mA g^{-1} in the 1.7–4.3 V vs. Na^+/Na. *Ex situ* XPS analysis reveals partial iron redox (Fe^{2+}/Fe^{3+}) activity. An *ex situ* experimental Raman spectroscopy study points to the presence of oxalate anion redox on cycling. The partial electronic density of states is also estimated to study the charge transfer between the different elements and highlight the iron and oxalate redox reactions. Finally, first-principles calculations of Bader charges provide further evidence of the importance of the oxalate group for the anionic redox processes during potassium extraction. Thus, the electrochemical activity of the oxalate group is non-negligible compared to the classical cationic iron redox behaviour and plays a prominent role in the charge compensation mechanism.

Conflicts of interest

There are no conflicts to declare.

Acknowledgements

Notes and references

1 J. Deng, W. Luo, S. Chou, H. Liu and S. Dou, *Adv. Energy Mater.*, 2018, **8**, 1701428.
2 Y. Niu, Y. Zhang and M. Xu, *J. Mater. Chem. A*, 2019, 7, 15006–15025.

3 M. H. Han, E. Gonzalo, G. Singh and T. Rojo, *Energy Environ. Sci.*, 2015, **8**, 81–102.

4 S. Guo, P. Liu, H. Yu, Y. Zhu, M. Chen, M. Ishida and H. Zhou, *Angew. Chem., Int. Ed.*, 2015, **54**, 5894–5899.

5 R. Rajagopalan, Y. Tang, C. Jia, X. Ji and H. Wang, *Energy Environ. Sci.*, 2020, **13**, 1568–1592.

6 B. Singh, Z. Wang, S. Park, B. Gopalakrishnan, S. Gautam, J.-N. El Chotard, L. Croguennec, D. Carlier, A. K. Cheetham, C. Masquelier and P. Canepa, *J. Mater. Chem. A*, 2021, **9**, 281–292.

7 B. Senthilkumar, C. Murugesan, L. Sharma, S. Lochab and P. Barpanda, *Small Methods*, 2019, **3**, 1–23.

8 S. W. Kim, D. H. Seo, X. Ma, G. Ceder and K. Kang, *Adv. Energy Mater.*, 2012, **2**, 710–721.

9 C. Berlanga, I. Monterrubio, M. Armand, T. Rojo, M. Galceran and M. Casas-Cabanas, *ACS Sustainable Chem. Eng.*, 2020, **8**, 725–730.

10 M. Law and P. Balaya, *Energy Storage Mater.*, 2018, **10**, 102–113.

11 H. Kim, G. Yoon, I. Park, K. Y. Park, B. Lee, J. Kim, Y. U. Park, S. K. Jung, H. D. Lim, D. Ahn, S. Lee and K. Kang, *Energy Environ. Sci.*, 2015, **8**, 3325–3335.

12 Q. Ni, L. Zheng, Y. Bai, T. Liu, H. Ren, H. Xu, C. Wu, C. Wu and J. Lu, *ACS Energy Lett.*, 2020, **5**, 1763–1770.

13 W. Pan, W. Guan, S. Liu, B. Bin Xu, C. Liang, H. Pan, M. Yan and Y. Jiang, *J. Mater. Chem. A*, 2019, **7**, 13197–13204.

14 H. Ahouari, G. Rousse, Y. Klein, J. N. Chotard, M. T. Sougrati, N. Recham and J. M. Tarascon, *Solid State Sci.*, 2015, **42**, 6–13.

15 W. Yao, M. T. Sougrati, K. Hoang, J. Hui, P. Lightfoot and A. R. Armstrong, *Chem. Mater.*, 2017, **29**, 9095–9101.

16 W. Yao, A. R. Armstrong, X. Zhou, M. T. Sougrati, P. Kidkhunthod, S. Tunmee, C. Sun, S. Sattayaporn, P. Lightfoot, B. Ji, C. Jiang, N. Wu, Y. Tang and H. M. Cheng, *Nat. Commun.*, 2019, **10**, 1–9.

17 W. Yao, M. T. Sougrati, K. Hoang, J. Hui, P. Lightfoot and A. R. Armstrong, *Chem. Mater.*, 2017, **29**, 2167–2172.

18 A. Pramanik, A. J. Bradford, S. L. Lee, P. Lightfoot and A. R. Armstrong, *J. Phys.: Mater.*, 2021, **4**, 24004.

19 W. Yao, Y.-Y. Guo and P. Lightfoot, *Dalton Trans.*, 2017, **46**, 13349.

20 R. Clulow, A. J. Bradford, S. L. Lee and P. Lightfoot, *Dalton Trans.*, 2019, **48**, 14461–14466.

21 H. He, W. Yao, S. Tunmee, X. Zhou, B. Ji, N. Wu, T. Song, P. Kidkhunthod and Y. Tang, *J. Mater. Chem. A*, 2020, **8**, 9128–9136.

22 R. B. Von Dreele, *J. Appl. Crystallogr.*, 1997, **30**, 517–525.

23 S. F. Linnell, E. J. Kim, Y.-S. Choi, M. Hirsbrunner, S. Imada, A. Pramanik, A. F. Cuesta, D. N. Miller, E. Fusco, B. E. Bode, J. T. S. Irvine, L. C. Duda, D. O. Scanlon and A. R. Armstrong, *J. Mater. Chem. A*, 2022, **10**, 9941–9953.

24 G. Kresse and J. Furthmu.

25 M. Perdew, J. P. Burke and K. Ernzerhof, *Phys. Rev. Lett.*, 1996, **77**, 3865–3858.

26 G. Kresse and D. Joubert, *Phys. Rev. B: Condens. Matter Mater. Phys.*, 1999, **59**, 1758–1775.

27 A. Jain, G. Hautier, S. P. Ong, C. J. Moore, C. C. Fischer, K. A. Persson and G. Ceder, *Phys. Rev. B: Condens. Matter Mater. Phys.*, 2011, **045115**, 1–10.

28 W. Tang, E. Sanville and G. Henkelman, *J. Phys.: Condens. Matter*, 2009, **21**, 7.

29 S. Li, X. Song, X. Kuai, W. Zhu, K. Tian, X. Li, M. Chen, S. Chou, J. Zhao and L. Gao, *J. Mater. Chem. A*, 2019, **7**, 14656–14669.

30 G. Yao, X. Zhang, Y. Yan, J. Zhang, K. Song, J. Shi, L. Mi, J. Zheng, X. Feng and W. Chen, *J. Energy Chem.*, 2020, **50**, 387–394.

31 H. Gao, S. Yan, J. Wang, Y. A. Huang, P. Wang, Z. Li and Z. Zou, *Phys. Chem. Chem. Phys.*, 2013, **15**, 18077–18084.

32 R. Sadri, M. Hosseini, S. N. Kazi, S. Bagheri, N. Zubir, K. H. Solangi, T. Zaharinie and A. Badarudin, *J. Colloid Interface Sci.*, 2017, **504**, 115–123.

33 M. K. Rabchinskii, A. T. Dideikin, D. A. Kirilenko, M. V. Baidakova, V. V. Shnitov, F. Roth, S. V. Konyakhin, N. A. Besedina, S. I. Pavlov, R. A. Kuricyn, N. M. Lebedeva, P. N. Brunkov and A. Y. Vul', *Sci. Rep.*, 2018, **8**, 1–11.

34 N. Khomiakova, J. Hanuš, A. Kuzminova and O. Kylián, *Coatings*, 2020, **10**, 619.

35 G. F. Meyers, M. B. Hall, J. W. Chinn and R. J. Lagow, *J. Am. Chem. Soc.*, 1985, **107**, 1413–1414.

36 X. Shan, F. Guo, D. S. Charles, Z. Lebens-Higgins, S. Abdel Razek, J. Wu, W. Xu, W. Yang, K. L. Page, J. C. Neuefeind, M. Feygenson, L. F. J. Piper and X. Teng, *Nat. Commun.*, 2019, **10**, 4975.

37 S. Ivanova, E. Zhecheva, R. Kukeva, D. Nihtianova, L. Mihaylov, G. Atanasova and R. Stoyanova, *ACS Appl. Mater. Interfaces*, 2016, **8**, 17321–17333.

38 P. Tang and N. A. W. Holzwarth, *Phys. Rev. B*, 2003, **68**, 165107.

39 P. Moreau, D. Guyomard, J. Gaubicher and F. Boucher, *Chem. Mater.*, 2010, **22**, 4126–4128.